Nano Research
2023, 16(7): 9591–9601

ISSN 1998-0124 CN 11-5974/O4
https://doi.org/10.1007/s12274-023-5776-x

Research Article

Enhancing electromagnetic wave absorption in carbon fiber using FeS_2 nanoparticles

Yuying Guo[1], Meng Zhang[1], Tingting Cheng[1], Yuxin Xie[1], Laibin Zhao[1], Liang Jiang[3], Wenxin Zhao[1], Liying Yuan[1], Alan Meng[2], Jian Zhang[2], Ting Wang[2] (✉), and Zhenjiang Li[1] (✉)

[1] *College of Electromechanical Engineering, Key Laboratory of Polymer Material Advanced Manufacturing's Technology of Shandong province, College of Materials Science and Engineering, Qingdao University of Science and Technology, Qingdao 266061, China*

[2] *College of Chemical Engineering, Key Laboratory of Optic-electric Sensing and Analytical Chemistry for Life Science, MOE, Shandong Key Laboratory of Biochemical Analysis, College of Chemistry and Molecular Engineering, Qingdao University of Science and Technology, Qingdao 266042, China*

[3] *College of Textiles and Clothing, Qingdao University, Qingdao 266071, China*

Received: 29 March 2023 / **Revised:** 21 April 2023 / **Accepted:** 24 April 2023

ABSTRACT

Carbon-based electromagnetic wave absorbing materials (absorbers) adhered with metallic sulfide nanoparticles of good electrical conductivity attract increasing researchers' attention. In this study, on the basis of carbon fiber (C_f)@Fe_3O_4 nanocomposites obtained by the electrostatic spinning and reflow method, C_f@FeS_2 nanocomposite was successfully prepared during a further hydrothermal process. The products exhibit excellent electromagnetic wave absorption performances with a minimum reflection loss (RL_{min}) of −54.11 dB at 2.13 mm matching thickness. At the same time, the optimal effective absorption bandwidth (EAB) value of 6.04 GHz at a thickness of 1.98 mm covers the whole Ku band, suggesting its excellent electromagnetic wave absorption performances. In addition, the interlaced network structure constructed by carbon fiber, outstanding conductivity of FeS_2 nanoparticles, and interfacial polarization from hetero-structure play significant parts in enhancing the electromagnetic parameters and absorption performances. All these results suggest that the C_f@FeS_2 nanocomposites can be taken as a new electromagnetic wave-absorbing material under their low density, simple craft, and strong absorption characteristics.

KEYWORDS

constructed network structure, carbon fiber (C_f)@FeS_2 nanocomposite, enhanced dielectric loss, microwave attenuation mechanism

1 Introduction

The rapid development and popularization of various electronic equipment in the past decade created great convenience for people. In the meanwhile, they also brought increasingly serious electromagnetic radiation problems [1–4]. As a result, people attach increasing importance to the research of electromagnetic wave absorbing materials (absorbers), especially absorbers with the characteristics of lightweight, thin coating, wide absorption frequency range, and strong attenuation capacity [5–8].

Among various candidate absorbers, carbon-based materials, including carbon nanotubes [9], carbon fiber (C_f) [10], graphene [11], and porous carbon [12], have shown extensive application prospects in the field of electromagnetic wave absorption depending on their advantages of good conductivity, low density, corrosion resistance, low cost, and abundant morphology besides excellent dielectric loss capacity [13]. Initially, one-dimensional carbon fiber is best known for its incomparable mechanical properties and flexible stretchability. With the in-depth research on microwave absorbing materials, its potential as lightweight absorbing material has been gradually tapped. Using polyacrylonitrile (PAN) and polymethyl methacrylate blends as precursors, Li et al. synthesized porous carbon fiber with the pore size of 0.1–1 μm and nanosize carbon fiber with the diameter of 100 nm, and the corresponding minimum reflection loss (RL_{min}) values are −31 and −12.2 dB, respectively [14]. Inspired by the microstructure of nepenthe, Huang et al. prepared spiral carbon fibers and recorded their microwave absorption properties with the RL_{min} of −30.67 dB at the thickness of 2.96 GHz [15]. Hu et al. investigated the electromagnetic wave absorption performances of carbon fibers prepared by the carbonization process, with the corresponding RL_{min} of −22.9 dB appearing at 15 GHz and the matching thickness of 2 mm [16]. Obviously, it is almost impossible to achieve satisfactory absorption performances based solely on the dielectric loss of carbon fibers.

Fortunately, it has been verified that combining carbon material with metallic components is a simple and feasible strategy to obtain an ideal absorber, which not only improves the impedance matching of bare carbon fiber but also causes addition dielectric loss, resulting in enhanced electromagnetic wave absorption performances [17–19]. More importantly, the interfacial polarization phenomenon occurs at the phase boundary of carbon-magnetic matter, which is also positive for the electromagnetic

Address correspondence to Ting Wang, wt@qust.edu.cn; Zhenjiang Li, zhenjiangli@qust.edu.cn

wave absorption performances [20–23]. C_f/FeCoNi hybrid material was successfully synthesized by Ye's team, when the RL_{min} of the sample was −30.62 dB, and the optimal effective absorption bandwidth (EAB) reached 7.4 GHz [24]. Qing et al. prepared Fe_3O_4/C_fs nanocomposite by the wet chemical method, and its RL_{min} value was −35 dB at 4.41 mm matching thickness [25]. Sun et al. produced active carbon fiber/Fe_3O_4 nanocomposites by the *in-situ* reduction method. Here, it should be noted that the RL_{min} of the carbon fiber was significantly improved by loaded Fe_3O_4 nanoparticles from −12.9 to −30.07 dB, and the corresponding optimal absorption bandwidth was 8.62 GHz at a matching thickness of 2 mm [26]. Zhou et al. successfully synthesized C@Fe_3O_4 nanocomposite material with a walnut shell as raw material and studied its absorbing performance. The reflection loss value is −40.3 dB when the matching thickness is 2.0 mm and the incident frequency is 17.5 GHz [27]. Due to the lower electronegativity of sulfur than oxygen, the ionic bond formed by transition metal sulfide has higher conductivity than transition metal oxides, and metal sulfide is featured with high activity and good chemical stability [28–30]. Among them, FeS_2 is non-toxic, cheap, and easy to prepare, and has a narrow band gap. Besides, it is used in the fields of electrode materials and catalysis for lithium, sodium, and magnesium plasma batteries, while little has been reported in the field of electromagnetic wave absorption. In this case, it can be inferred that decorating transition metal (FeS_2) on the surface of carbon materials can promote charge transfer, enhance the conductivity of materials, and improve the absorption performance of C_f to a great extent.

In this study, bare C_f and C_f@Fe_3O_4 nanocomposites were subsequently prepared by electrospinning technique and reflux process. Subsequently, the C_f@FeS_2 nanocomposite was successfully produced by experiencing a hydrothermal sulfide process. The electromagnetic parameters and corresponding absorption properties of the products were measured and investigated carefully. According to the systematic characterization results, a reasonable mechanism was established to demonstrate the attenuation process of incident electromagnetic waves.

2 Experimental section

2.1 Materials

Polyacrylonitrile (analytical purity), N,N-dimethylformamide (DMF, analytical purity), ferric nitrate nine-water ($Fe(NO_3)_3{\cdot}9H_2O$, analytical purity), urea (analytical purity), and thioacetamide (TAA, analytical purity) were provided by Sinopharm Chemical Reagent Co., Ltd. All raw materials were employed directly without further purification treatment.

2.2 Preparation of precursor PAN nanofiber

Firstly, the light yellow precursor spinning solution with a mass fraction of 10 wt.% was prepared through magnetic stirring for 2 h at 60 °C using PAN and DMF as solute and solvent, respectively. After that, the solution was poured into a syringe connected to a micro-injection pump. Subsequently, the positive and negative electrodes of an applied high-voltage power were matched with the needle of the syringe and receiving copper plate, respectively. The relevant parameters were controlled as follows: The voltage was constant at 15 kV, while the spacing between positive and negative electrodes was kept at 15 cm, and the feeding rate of the solution was fixed at approximately 0.8 mL/h. A dozen hours later, cotton-like PAN fibers were easily stripped from the cooper plate.

2.3 Preparation of C nanofiber cloth

The collected PAN precursor fibers were dried entirely in a vacuum oven for 12 h at 60 °C. Then, a pre-oxidation treatment process was exerted to maintain its original shape. The prepared sample was placed in a muffle furnace, heated to 280 °C, and held for 1 h at a heating rate of 1 °C/min. Afterwards, the treated fibers were further carbonized in an inert atmosphere at 700 °C for 30 min with an increasing rate of 5 °C/min. Finally, netlike C nanofiber cloth was prepared.

2.4 Preparation of C_f@Fe_3O_4 nanocomposites

Firstly, 1 g $Fe(NO_3)_3{\cdot}9H_2O$ and 1 g urea were evenly dispersed in 200 mL deionized water. Then, 1 g C_f nanofiber cloth was injected into the solution and refluxed at 120 °C for 6 h, followed by the fabric being rinsed with deionized water at ambient temperature and dried at 60 °C. Finally, the target product, C_f@Fe_3O_4 nanocomposite, was prepared by annealing treatment in an inert atmosphere at 500 °C for 6 h at an increasing rate of 2 °C/min. By adjusting the total amount of $Fe(NO_3)_3{\cdot}9H_2O$ and urea but maintaining their ratio, the content of Fe_3O_4 nanoparticles could be changed, and the corresponding products are labeled as C_f@Fe_3O_4-1#, C_f@Fe_3O_4-2#, and C_f@Fe_3O_4-3#, respectively.

2.5 Preparation of C_f@FeS_2 nanocomposite

0.3 g C_f@Fe_3O_4 nanocomposites and 0.75 g TAA were dissolved in 80 mL deionized water, stirred for 2 h on a magnetic stirrer for uniform mixing, then placed in the lining of a 100 mL reaction kettle, and afterwards put in the oven for hydrothermal reaction at 200 °C for 12 h. After cooled, the powder was removed from the reaction kettle. In the end, C_f@FeS_2 nanocomposite was obtained by centrifugal drying. The synthesis process is illustrated in Fig. 1(a).

2.6 Material characterization

X-ray diffraction (XRD) on Bruker D8 advance was used to detect the phase structure information. Renishaw 2000 micro-Raman system was employed to investigate the structure property of the sample. Scanning electron microscopy (SEM) of Hitachi S-4800 was used to analyze the morphology information of the products. The hysteresis loop was measured by a vibrating sample magnetometry (VSM, Quantum Design PPMS-9) at room temperature to evaluate the magnetic properties of C_f@Fe_3O_4 nanocomposites. The surface element composition and chemical bonding state of the nanocomposites were measured by X-ray photoelectron spectroscopy (XPS, Thermo ESCALAB 250XI). The microstructure could be confirmed by a transmission electron microscopy (TEM, Hitachi H-8100). Thermogravimetric analysis (TGA) of the samples was carried out in air with a heating rate of 5 °C/min. All prepared samples were mixed with paraffin wax to measure the electromagnetic parameters. The ring sample had a filling content of about 30 wt.% and outer and inner diameters of 7 and 3.04 mm, respectively. The vector network analyzer (Agilent, N5230A) was used to measure the complex permittivity and permeability of the samples in 2–18 GHz frequency range.

3 Results and discussion

XRD was employed to analyze the crystal structure and phase composition of the as-obtained sample, and the corresponding pattern is shown in Fig. 1(b). Two broad diffraction peaks appearing at 26° and 42° are consistent with (002) and (100) lattice planes of carbon, respectively [31]. To evaluate the defect degree of carbon, Raman spectra were measured. Figure 1(c) exhibits the Raman spectrum of the as-prepared C_f, in which the typical character peaks around 1355 and 1595 cm^{-1} can be ascribed to the D band and G band of the carbon structure, reflecting the lattice defect and the in-plane stretching vibration of the sp^2 hybrid of C

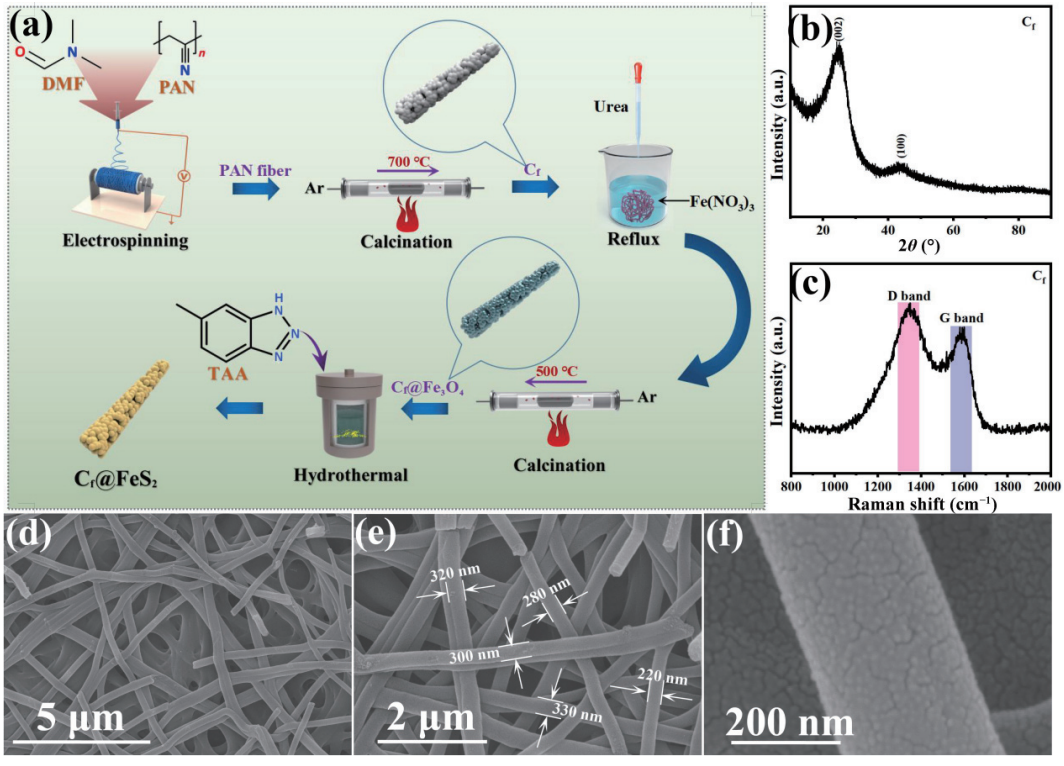

Figure 1 (a) Schematic illustration of the preparation process of C_f@FeS_2 nanocomposites. (b) XRD pattern and (c) Raman spectrum of the prepared carbon fibers sample. (d)–(f) SEM images of the as-prepared carbon fibers.

atom, accordingly [32, 33]. In addition, the integral area ratio concerning the D band and G band (A_D/A_G) of C_f is about 2.72, suggesting many lattice defects in the sample [34]. As revealed in Figs. 1(d)–1(f), from the SEM images of C_f, it can be observed that the diameter of an isolated sample with a smooth surface is about 220–330 nm, and the length reaches dozens of microns. Furthermore, some adjacent C_f overlapped and interlaced with each other to construct a network structure.

The morphology of C_f@Fe_3O_4 nanocomposites was observed by the scanning electron microscopy. In Figs. 2(a) and 2(b), the SEM images of the C_f@Fe_3O_4-1# nanocomposites are shown. The surface of the sample becomes rough after successfully decorating numerous tiny Fe_3O_4 nanoparticles on the surface of C_f, and at the same time, the corresponding diameter of the sample increases. For C_f@Fe_3O_4-2# and C_f@Fe_3O_4-3# nanocomposites, it can be found that more Fe_3O_4 nanoparticles are uniformly anchored on the surface of the obtained C_f, and the maximum diameter increases to approximately 600 nm, as revealed in Figs. 2(c)–2(f). The phase composition of the sample was analyzed by XRD, while Fig. 2(g) displays the XRD patterns of the C_f@Fe_3O_4 nanocomposites, and the weak relative peak intensity indicates the amorphous state of C_f. Besides the above diffraction peaks of carbon, other obvious character peaks located at 18.3°, 30.1°, 35.6°, 43.2°, 53.5°, 57.1°, and 62.7° correspond to (111), (220), (311), (400), (422), (511), and (440) lattice planes of Fe_3O_4 (JCPDS No. 79-0419) respectively [35, 36]. It can be further confirmed that Fe_3O_4 magnetic particles have successfully adhered to the surface of C_f. The diffraction peak intensity of C_f@Fe_3O_4 nanocomposites increases gradually with the reflux solution concentration, implying that more Fe_3O_4 particles can be obtained. Beyond that, Fig. 2(h) shows the Raman spectra of the Fe_3O_4 nanocomposites. A_D/A_G ratios of various samples are 2.31, 2.80, and 2.83 separately, suggesting that the carbon-related defect increases gradually with the content increase of Fe_3O_4 nanoparticles. The ferromagnetism of C_f@Fe_3O_4 nanocomposites at room temperature was investigated using VSM, and the corresponding hysteresis loops are shown in Fig. 2(i). It is well known that the saturation magnetization and coercivity are significant indexes for evaluating the magnetic matter [37, 38]. Since decorating the highest content of Fe_3O_4 nanoparticles, the C_f@Fe_3O_4-3# nanocomposite obtains the maximum saturation magnetization and minimum coercivity values. The saturation magnetization values of C_f@Fe_3O_4-1#, C_f@Fe_3O_4-2#, and C_f@Fe_3O_4-3# samples are 23.03, 33.70, and 41.52 emu/g, respectively. Figure S1 in the Electronic Supplementary Material (ESM) exhibits a partially enlarged detail of Fig. 2(i). The coercivity value of C_f@Fe_3O_4-1# is 173.32 Oe, which is higher than that of C_f@Fe_3O_4-2# and C_f@Fe_3O_4-3# nanocomposites. In addition, the residual magnetization values of C_f@Fe_3O_4-1#, C_f@Fe_3O_4-2#, and C_f@Fe_3O_4-3# samples are 7.07, 9.09, and 9.91 emu/g, accordingly, demonstrating that the increased Fe_3O_4 nanoparticles endow the C_f with more robust magnetic properties. Moreover, XPS characterization was employed to further detect the elemental composition and chemical bond state of the C_f@Fe_3O_4 nanocomposite, and the representative results are exhibited in Figs. 2(j)–2(l). Figure S2 in the ESM presents the XPS full spectrum of the synthesized C_f@Fe_3O_4 nanocomposite, in which C, O, and Fe elements can be obviously marked. Deservedly, the C element can be assigned to C_f, and Fe and O elements come from Fe_3O_4 nanoparticles. As Fig. 2(j) shows, three peaks can be stripped from the C 1s spectra, and the binding energies existing at 284.8, 286.4, and 288.4 eV correspond to the C–C bond, C–O bond, and C=O bond, respectively [39]. Figure 2(k) is the O 1s spectra, and the peak can be separated into two split peaks centered at 530.4 and 532.1 eV, namely Fe–O and C=O [40]. In the Fe 2p spectra (Fig. 2(l)), several peaks appear in pairs at 708.3 and 721.2 eV, and 710.1 and 724.3 eV, respectively, which may be aroused by the characteristics of Fe^{2+} and Fe^{3+} [41].

As is known to all, four parameters, the real part and the imaginary part of the complex permittivity ($\varepsilon_r = \varepsilon' - j\varepsilon''$) and complex permeability ($\mu_r = \mu' - j\mu''$) are key parameters in the absorption properties of the absorber [42–44]. The electromagnetic parameters of the C_f and C_f@Fe_3O_4 nanocomposites vary with frequency, as shown in Figs. 3(a), 3(b),

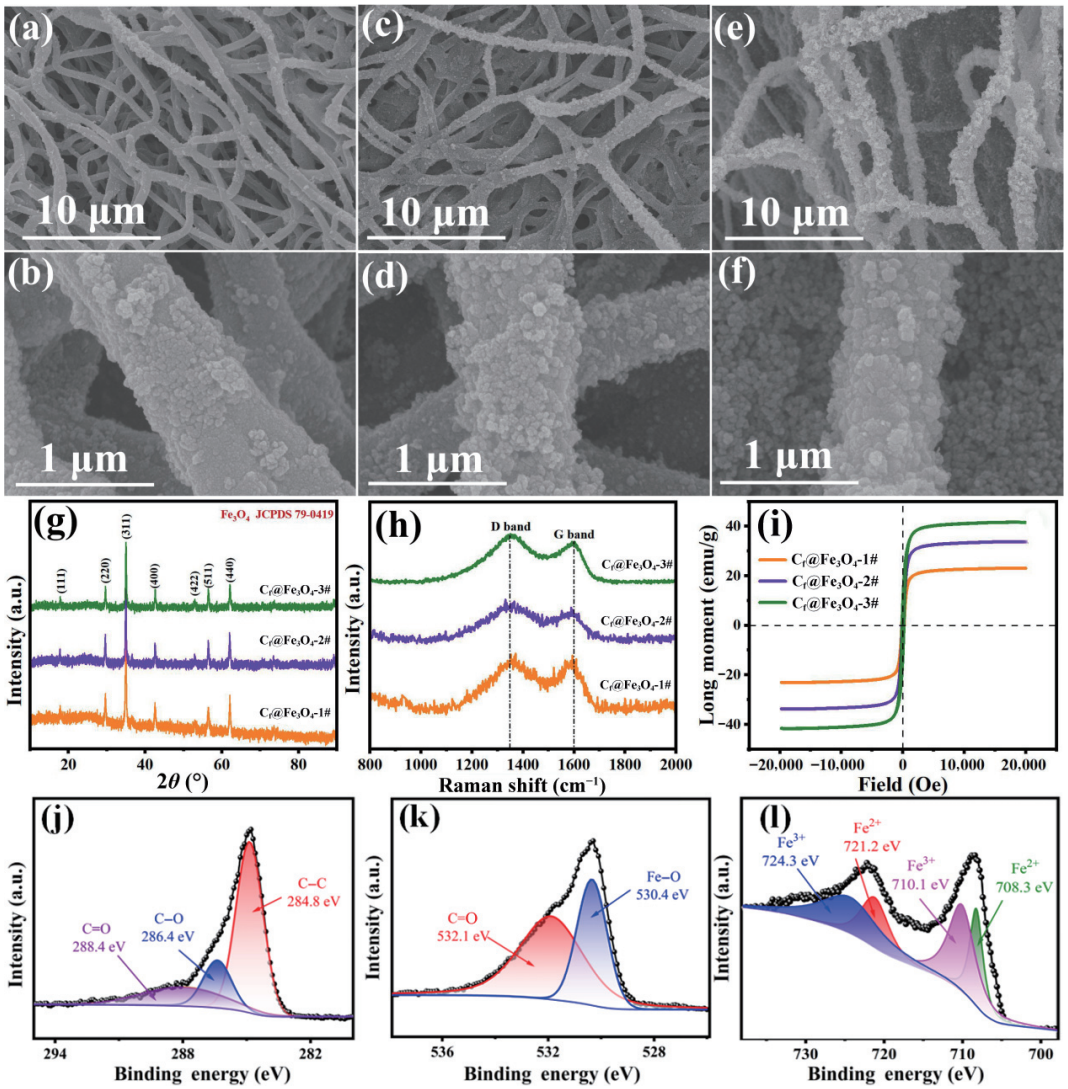

Figure 2 SEM images of ((a) and (b)) $C_f@Fe_3O_4$-1#, ((c) and (d)) $C_f@Fe_3O_4$-2#, and ((e) and (f)) $C_f@Fe_3O_4$-3# nanocomposites. (g) XRD patterns, (h) Raman spectra, and (i) magnetic hysteresis loops of the $C_f@Fe_3O_4$ nanocomposites at room temperature. High-resolution (j) C 1s, (k) O 1s, and (l) Fe 2p spectra of typical $C_f@Fe_3O_4$ nanocomposites.

3(d), and 3(e). Figures 3(a) and 3(b) present the ε' and ε'' curves of C_f and $C_f@Fe_3O_4$ nanocomposites, respectively. Generally, the ε' and ε'' values of $C_f@Fe_3O_4$ nanocomposites are higher than those of C_f in the measured frequency range. Noteworthy, the ε' value of $C_f@Fe_3O_4$-3# nanocomposite ranges from 5.56 to 9.25, displaying a downward trend in the 2–16 GHz frequency and an upward trend in the 16–18 GHz frequency, which is also higher than that of $C_f@Fe_3O_4$-1# and $C_f@Fe_3O_4$-2# nanocomposites. In Fig. 3(b), compared with C_f, several resonance peaks appear around 9.5, 12.5, and 14.5 GHz in the $C_f@Fe_3O_4$-3# nanocomposites, reflecting the polarization effect of Fe_3O_4 nanoparticles at these frequency locations, which may significantly improve the attenuation for electron filed incident electromagnetic wave energy. Figures 3(d) and 3(e) reveal the variation tendency of μ' and μ'' values with the varied frequency of C_f and $C_f@Fe_3O_4$ nanocomposites. Due to its non-magnetic character, the μ' and μ'' values of C_f fluctuate within a narrow range around 1 and 0. Among all the three $C_f@Fe_3O_4$ nanocomposite samples, the μ' curve of $C_f@Fe_3O_4$-1# nanocomposite reaches the maximum value of 1.44 at 13.6 GHz. Apart from that, $C_f@Fe_3O_4$-2# nanocomposite is featured with the maximum μ'' value and multiple resonance peaks in the 2–18 GHz frequency range, suggesting its excellent attenuation loss for the magnetic field of incident microwave energy. The μ'' curve of $C_f@Fe_3O_4$-3# nanocomposites shows a downward trend in the 2–15 GHz frequency range and an upward trend in the 15–18 GHz frequency range. Figures 3(c) and 3(f) display the dielectric loss tangent and magnetic loss tangent of C_f and $C_f@Fe_3O_4$ nanocomposites, which are similar to the varying imaginary part of the permittivity and permeability. In addition, the values of dielectric loss tangent are more prominent than those of magnetic loss tangent in the most frequency ranges, meaning that the dielectric loss mechanism mainly dominates the attenuation process of the electromagnetic wave.

According to transmission line theory, the electromagnetic wave absorption performances of an absorbing material can be expressed by the RL value. In general, the RL value of the sample can be collected by Eqs. (1) and (2) [45, 46]

$$\mathrm{RL}\,(\mathrm{dB}) = 20\log\left|\frac{Z_{\mathrm{in}} - Z_0}{Z_{\mathrm{in}} + Z_0}\right| \tag{1}$$

$$Z_{\mathrm{in}} = Z_0\sqrt{\frac{\mu_{\mathrm{r}}}{\varepsilon_{\mathrm{r}}}}\tanh\left[\mathrm{j}\left(\frac{2\pi fd}{c}\right)\sqrt{\mu_{\mathrm{r}}\varepsilon_{\mathrm{r}}}\right] \tag{2}$$

where Z_0 is the impedance in free space, Z_{in} denotes the input impedance, f refers to the frequency, d signifies the absorber matching thickness, ε_{r} and μ_{r} stand for the complex permittivity and permeability, respectively, and c is equal to the speed of light. Here, it should be noted that the effective absorption bandwidth value (RL value < −10 dB) is usually employed to evaluate the

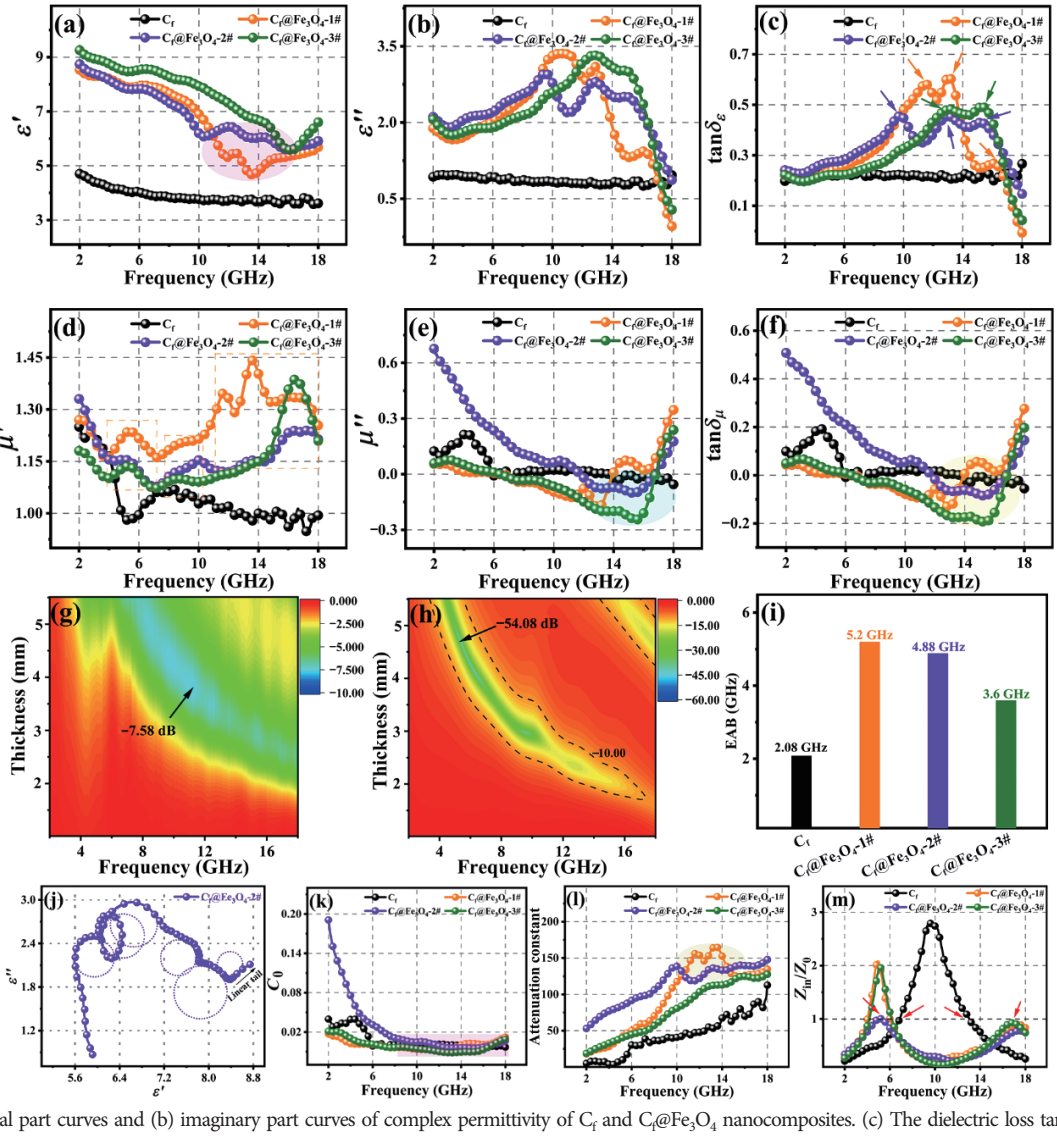

Figure 3 (a) Real part curves and (b) imaginary part curves of complex permittivity of C_f and $C_f@Fe_3O_4$ nanocomposites. (c) The dielectric loss tangent of C_f and $C_f@Fe_3O_4$ nanocomposites. (d) Real part curves and (e) imaginary part curves of complex permeability of C_f and $C_f@Fe_3O_4$ nanocomposites. (f) The magnetic loss tangent of C_f and $C_f@Fe_3O_4$ nanocomposites. RL values versus frequency of (g) C_f and (h) $C_f@Fe_3O_4$-2# nanocomposite at different thicknesses. (i) Comparison of EAB values of C_f and $C_f@Fe_3O_4$ nanocomposites. (j) Cole–Cole curve of the $C_f@Fe_3O_4$-2# nanocomposite. (k) C_0 curves, (l) attenuation constant, and (m) impedance matching of C_f and $C_f@Fe_3O_4$ nanocomposites.

feasibility of absorbing material in different frequency ranges, meaning 90% of the incident electromagnetic waves can be attenuated by the absorber [47]. Figure 3(g), and Figs. S3(a) and S3(b) in the ESM reveal the reflection loss of C_f samples in the frequency range of 2–18 GHz versus matching thicknesses. It can be discovered that the RL_{min} of C_f is −7.58 dB at a matching thickness of 4.0 mm, which fails to meet the effective absorption standard, indicating its inferior absorption performance. For $C_f@Fe_3O_4$-1# nanocomposite (Figs. S3(c) and S3(d) in the ESM), a small number of Fe_3O_4 nanoparticles improve the absorption performances of C_f whose RL_{min} value is −23.02 dB appearing at 16.8 GHz when the thickness is 5.0 mm. Its widest effective absorption bandwidth is about 4.80 GHz at a matching thickness of 2.5 mm. Figure 3(h), and Figs. S3(e) and S3(f) in the ESM exhibit the reflection loss values of $C_f@Fe_3O_4$-2# nanocomposites with the RL_{min} value of −54.08 dB at 5.28 GHz, and the corresponding matching thickness is 4.75 mm. Meanwhile, an optimal effective absorption bandwidth of 3.68 GHz has been obtained at the matching thickness of 2.96 mm, almost covering the entire X-band, manifesting its good absorption performance. However, with a further increase of Fe_3O_4 nanoparticle content, the absorption performances of the $C_f@Fe_3O_4$-3# nanocomposites decrease sharply with the RL_{min} value of −25.12 dB at nearly 18 GHz while the matching thickness is 4.5 mm, revealing that excessive Fe_3O_4 nanoparticles may adversely affect the absorption properties. In order to investigate the wave absorption performance of C_f and $C_f@Fe_3O_4$ nanocomposites more intuitively, the corresponding RL_{min} values of the samples and optimal EAB values were summarized and compared, as shown in Fig. 3(i) and Fig. S4 in the ESM. Then, it can be seen that the order of RL values of various samples is generally consistence with the values of complex permeability. In addition to that, the primary attenuation of incident electromagnetic waves occurs in the Ku band, which seems to have nothing to do with the number of magnetic Fe_3O_4 nanoparticles.

Debye relaxation theory is conducive to exploring the dielectric loss mechanism and relaxation process from the absorber, which can be acquired according to Eq. (3) [48]

$$\left(\varepsilon' - \frac{(\varepsilon_s + \varepsilon_\infty)}{2}\right)^2 + (\varepsilon'')^2 = \left(\frac{\varepsilon_s - \varepsilon_\infty}{2}\right)^2 \quad (3)$$

where ε_s and ε_∞ correspond to the static dielectric constant and static dielectric constant at the high-frequency limitation, respectively. Generally, in the curve of ε' versus ε'', each semicircle

stands for a Debye polarization relaxation process. Figure S5 in the ESM displays the Cole–Cole curves of C_f and C_f@Fe_3O_4 nanocomposites. As shown in Fig. S5(a) in the ESM, just two circles can be marked for the C_f, suggesting that the bare carbon material cannot produce a strong polarization loss effect and plays a minimal role in attenuating electromagnetic waves. After decorating Fe_3O_4 nanoparticles, the C_f@Fe_3O_4 nanocomposites obtain additional Debye relaxation processes induced by the interface between C and Fe_3O_4 apart from retaining the original loss effect of carbon fibers and displaying more circles, especially for C_f@Fe_3O_4-2# nanocomposite (as exhibited in Fig. 3(j)). Moreover, a linear tail is displayed at the end of the C_f@Fe_3O_4 nanocomposite curve, which may be related to the enhanced conduction loss of the product to some degree.

Generally, the combined action of natural resonance and exchange resonance mainly caused the magnetic loss of C_f@Fe_3O_4 nanocomposites. The effect of available eddy current on magnetic loss could be expressed by the C_0 curve. Based on the transmission line theory, C_0 could be calculated by Eq. (4) [49, 50]

$$C_0 = \mu''(\mu')^{-2} f^{-1} \quad (4)$$

Figure 3(k) shows the C_0 curves of C_f and C_f@Fe_3O_4 nanocomposites calculated in the frequency range of 2–18 GHz. As C_f is a typical dielectric loss absorber and almost no magnetic loss can be produced, the curve of C_f remains nearly constant without fluctuation. Besides, the C_0 values of C_f@Fe_3O_4-1# and C_f@Fe_3O_4-3# nanocomposites are constant because of the low magnetic loss, whereas the C_0 value of C_f@Fe_3O_4-2# nanocomposites gradually decreases in the frequency range of 2–7 GHz, revealing that the magnetic loss results from natural resonance. In addition, slight fluctuations of C_0 value in 16–18 GHz indicate that exchange resonances lead to magnetic losses. Furthermore, the attenuation constant (α) is usually adopted to evaluate the attenuation capacity of absorbing material, which can be expressed as Eq. (5) [51]

$$\alpha = \frac{\sqrt{2}\pi f}{c}\sqrt{(\mu''\varepsilon'' - \mu'\varepsilon') + \sqrt{(\mu''\varepsilon'' - \mu'\varepsilon')^2 + (\mu'\varepsilon'' + \mu''\varepsilon')^2}} \quad (5)$$

In Fig. 3(l), it can be seen that the α value of C_f@Fe_3O_4-2# nanocomposite is more significant than that of C_f@Fe_3O_4-1# and C_f@Fe_3O_4-3# nanocomposites, and all of them are greater than C_f, indicating the strong attenuation capability of C_f@Fe_3O_4 nanocomposites for incident electromagnetic waves. Other than that, impedance matching reflects the number of electromagnetic waves introduced into the absorber. Ideally, the impedance matching value should be close to 1, suggesting that the microwave enters the absorbing material completely without any reflection [52]. Figure 3(m) shows the impedance matching curves of C_f and C_f@Fe_3O_4 nanocomposites at their optimal thickness of themselves. In addition, C_f@Fe_3O_4-2# nanocomposite achieves a Z_{in}/Z_0 value of 1 at the RL_{min} located frequency, implying better impedance matching.

The XRD pattern can show the phase structure and crystallinity of the sample. Figure 4(a) displays the XRD pattern of C_f@FeS_2. It can be clearly seen that several diffraction peaks appear around 33.0°, 37.1°, 40.7°, 47.4°, 56.2°, 61.6°, and 64.2°, which match well with the standard pattern (JCPDS No. 42-1340) of FeS_2 and are assigned to the crystal planes (200), (210), (211), (220), (311), (023), and (321) [53, 54]. It is also indicated that the Fe_3O_4 nanoparticles adhered to C_f have been successfully converted into FeS_2. Moreover, the weaker relative strength of the samples can be attributed to the shedding of some alloy nanoparticles during the vulcanization process. Figure 4(b) presents the Raman spectrum of the C_f@FeS_2 nanocomposite. The integrated area of the D and G bands can be calculated by Gaussian fitting to be 2.73, demonstrating carbon-related defects in the sulfide product C_f@FeS_2 nanocomposites. Figures 4(c)–4(e) exhibit the SEM images of the C_f@FeS_2 nanocomposite. It can be seen that there is no obvious change in the structure of the constructed network, and the coating wrapped outside of the C_f changes from granular to burr-like ones, evenly distributing on C_f, and the diameter of C_f has changed slightly, remaining at about 500 nm. Besides, to further determine the constituent elements of the vulcanization product, the sample was analyzed using XPS technology. The C_f@FeS_2 in Fig. 4(f) exhibits four distinct peaks corresponding to S, C, O, and Fe elements, respectively, and the presence of S verifies the successful synthesis of FeS_2. Moreover, the peak fitting of the S 2p orbit is presented in Fig. 4(g), and it can be clearly known that the peak at 168.9 eV is related to SO_x, while the peak at 163.8 eV can be assigned to the S–Fe bond, and that at 162.6 eV is attributed to S $2p_{1/2}$ [55, 56]. In Fig. 4(h), two peaks can be divided in the O 1s spectra, the peak at 530 eV corresponds to the C=O bond, and that at 531.1 eV corresponds to the C–O bond [57]. Figure 4(i) exhibits the spectra of Fe 2p, and the Fe $2p_{1/2}$ (723.3 eV) and Fe $2p_{1/2}$ (705.6 eV) demonstrate the presence of Fe^{2+} [58, 59]. Figure 4(j) is the spectra of the C 1s peak. Three splitting peaks at 284.6, 286.1, and 287.9 eV can be ascribed to C–C, C–O, and C=O bonding, respectively [60, 61]. In Fig. S6 in the ESM, there is the TGA curve that shows the mass variation of C_f@FeS_2 nanocomposite treated in air atmosphere with the heating temperature ranging from 30 to 700 °C. In this case, it can be seen that two distinct mass changes exist in the curve. In the temperature range from room temperature to 430 °C, the mass slowly decreases with increasing temperature, and it can be assumed that this stage corresponds to the escape of some adsorbed water or functional groups from the product, accompanied by the oxidation of a small amount of carbon [62], and the weight change is about 4.64 %. In the range of 430 to 675 °C, a sharp decrease in mass occurs, with a mass loss of about 60.82%, which corresponds to both the further oxidation of carbon fibers and the transformation of FeS_2 into Fe_2O_3 [63]. It can be deduced that the mass fraction of residual Fe_2O_3 is 34.14 wt.%. Therefore, the mass fraction of FeS_2 in the product is approximately 51.21 wt.%, and that of C fiber is 48.79 wt.%.

A typical TEM characterization result of the C_f@FeS_2 nanocomposite is shown in Fig. 5. As indicated in Fig. 5(a), in the low-magnification image, there is an apparent difference between bright and shade contrast at different locations, where the bright region corresponds to the amorphous C_f and the dark region (as indicated by the red arrow) corresponds to the FeS_2 nanoparticles, respectively. The energy dispersive X-ray spectroscopy (EDS) spectrum corresponding to the sample is shown in the upper right inset of Fig. 5(a), where the presence of C, Fe, and S elements can be detected, and the other peaks can be caused by the copper mesh employed for the test. Figures 5(b) and 5(g) are high-magnification images collected from different sample areas, which display some tiny particles uniformly dispersed on the surface of C_f besides the large-grained FeS_2 (as indicated by the red dashed area). Figues 5(d)–5(f) reveal the C, Fe, and S element mapping images acquired from the sample in Fig. 5(b), verifying that the product is composed of C fiber and anchored FeS_2 nanoparticles. In order to investigate the lattice structure of the products, high-resolution TEM (HRTEM) characterization was exerted at different regions, and Figs. 5(h)–5(j) were captured from the corresponding marked regions in Figs. 5(b) and 5(g), respectively. Then, it can be found that each grain has different growth directions, where the crystalline plane spacings of 0.270, 0.242, 0.221, 0.192, 0.163, 0.150, and 0.145 nm correspond to (200), (210), (211), (220), (311), (023), and (321) crystal planes of FeS_2,

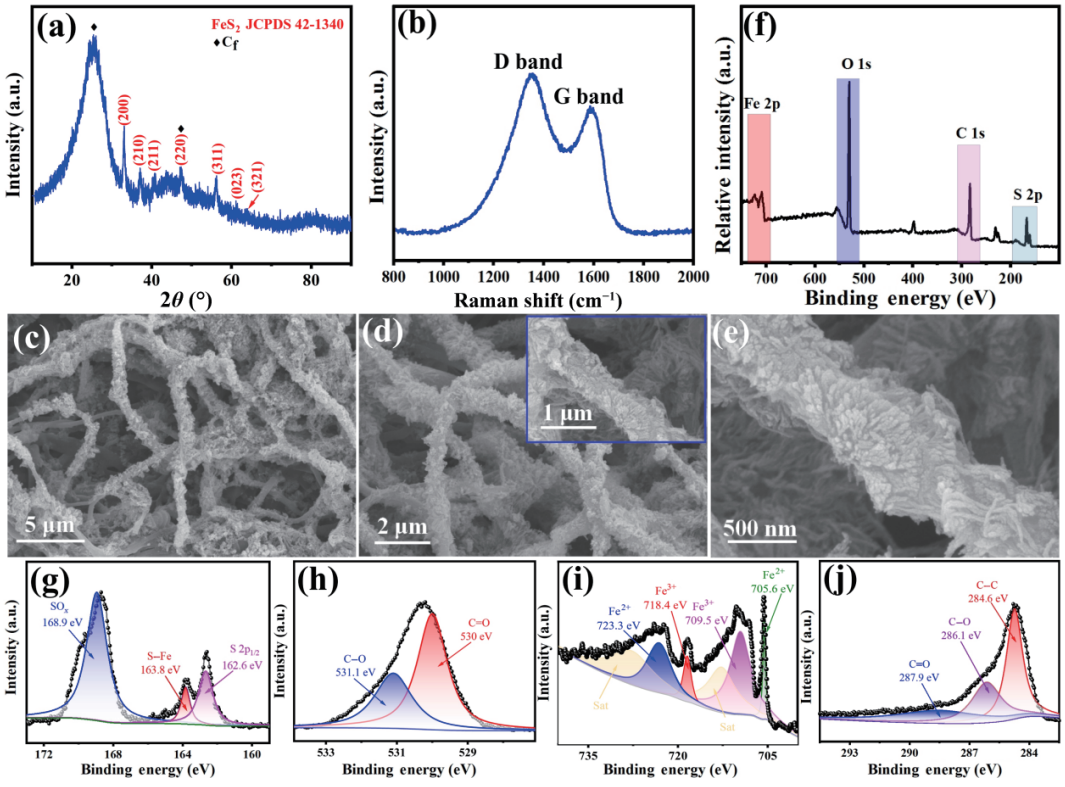

Figure 4 (a) XRD pattern and (b) Raman spectrum of the C_f@FeS_2 nanocomposite. (c)–(e) SEM images of the C_f@FeS_2 nanocomposite. (f) XPS full spectrum and high-resolution (g) S 2p, (h) O 1s, (i) Fe 2p, and (j) C 1s spectra of the C_f@FeS_2 nanocomposite.

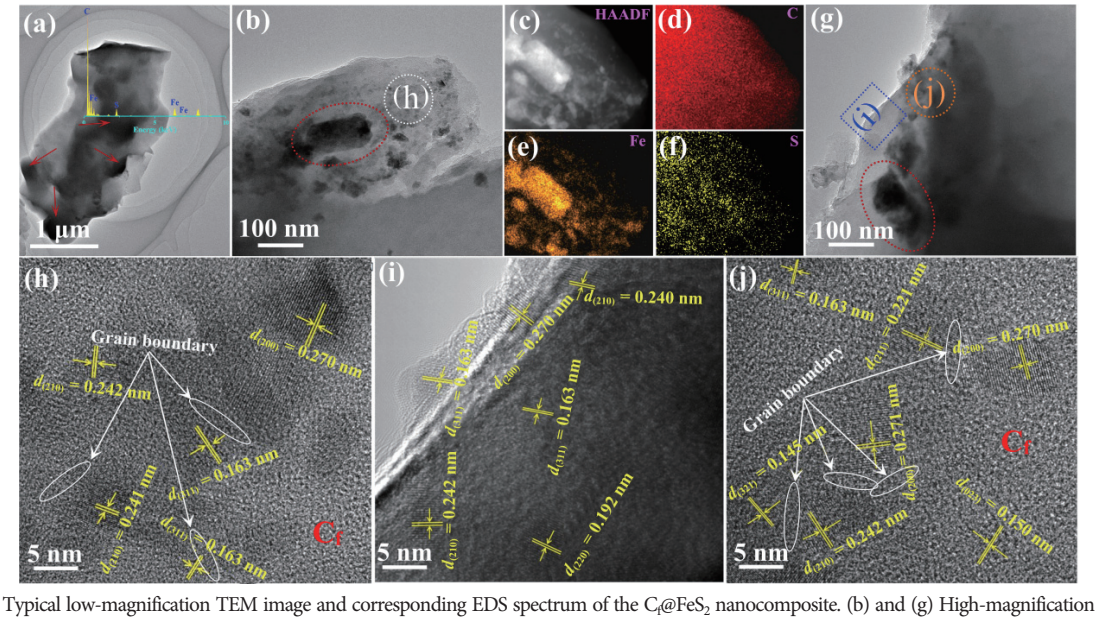

Figure 5 (a) Typical low-magnification TEM image and corresponding EDS spectrum of the C_f@FeS_2 nanocomposite. (b) and (g) High-magnification TEM images. (c) High-angle annular dark field (HAADF) image and (d)–(f) C, Fe, and S element mapping images captured from (b). (h)–(j) Corresponding HRTEM images collected from (b) and (g).

respectively. In addition, it can be held that there are obvious grain boundaries between the adjacent grains (as shown by the arrows and white oval regions in Figs. 5(h) and 5(j)), which may accumulate a large amount of charge under the action of an applied electric field, causing significant interfacial polarization and contributing to the attenuation of electromagnetic waves.

Figure 6(a) shows the real part and imaginary part curves concerning the complex permittivity of the C_f@FeS_2 nanocomposite. As exhibited in the figure, the real part curve slightly fluctuates around 10 GHz in the frequency range of 2–13 GHz, meanwhile, the corresponding values display a downward trend with multiple vibration peaks in the frequency range of 13–18 GHz. The imaginary part remains constant in low frequencies, showing a trend of rising and falling in the frequency range of 8–18 GHz, which reaches a maximum value of 6.81 at 14.48 GHz, implying that C_f@FeS_2 nanocomposites have good dielectric loss ability. Noteworthily, the values of the real part and the imaginary part are basically the same in the Ku band, indicating that the product possesses good impedance matching ability. Since FeS_2 is not a magnetic material, the magnetic loss of the C_f@FeS_2 nanocomposites is generally considered almost negligible. Figure S7 in the ESM displays the dielectric loss of C_f@FeS_2 nanocomposites, where multiple vibration peaks appear at high frequencies. As FeS_2 has no magnetic loss, the absorption attenuation of the C_f@FeS_2 is dominated by dielectric loss. Figure 6(b) and Fig. S8 in the ESM display the RL values of C_f@FeS_2

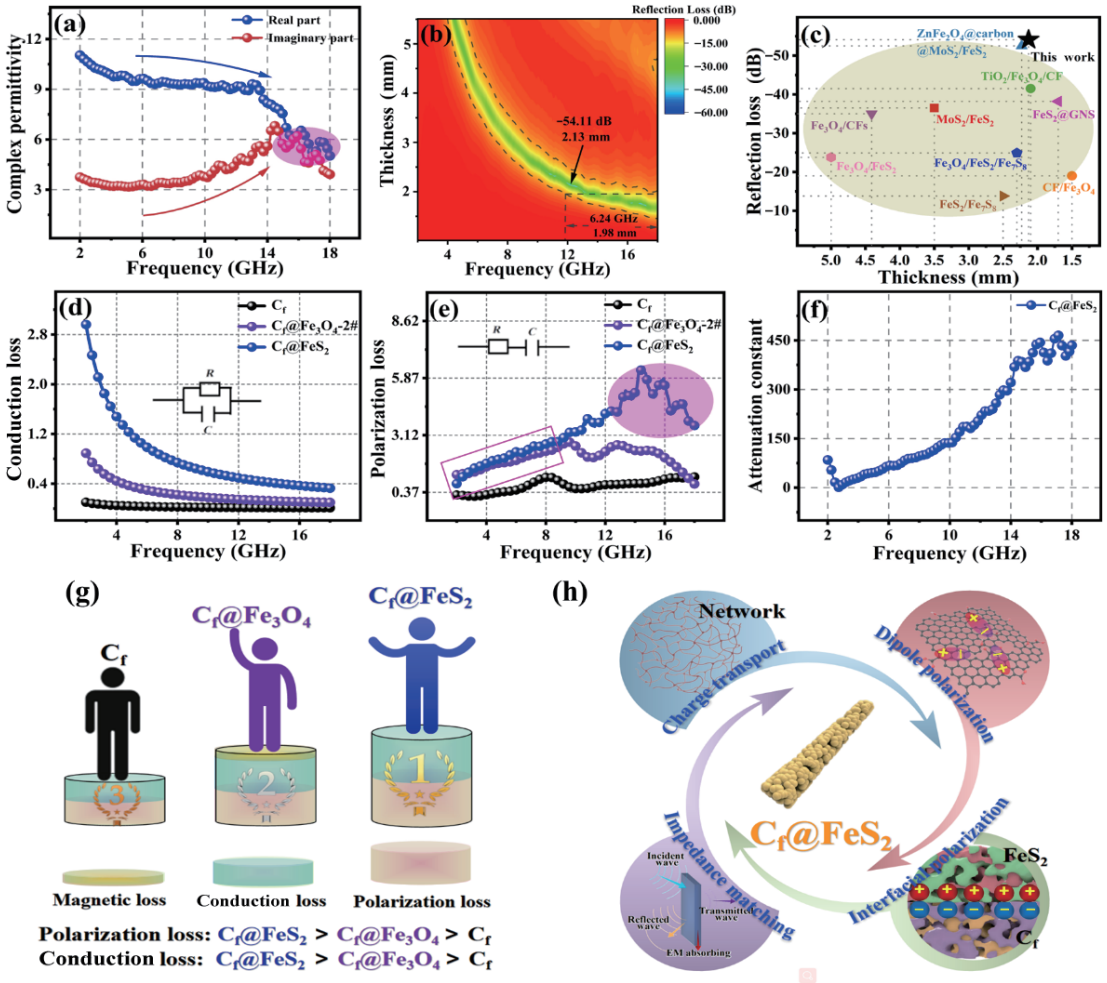

Figure 6 (a) Real part and imaginary part values of complex permittivity of the C_f@FeS_2 nanocomposites. (b) RL value versus frequency of the C_f@FeS_2 nanocomposite at different thicknesses. (c) Comparison of the minimum RL values of the C_f@FeS_2 with other nanocomposites reported recently. (d) Conduction loss values and (e) polarization loss values of C_f, C_f@Fe_3O_4-2#, and C_f@FeS_2 nanocomposites. (f) Attenuation constant of the C_f@FeS_2 nanocomposites. (g) and (h) Schematic diagrams of electromagnetic wave attenuation approaches of C_f@FeS_2 nanocomposites.

nanocomposites versus thickness and frequency. It can be clearly seen that C_f@FeS_2 obtains excellent electromagnetic wave absorption performance. When the matching thickness is 2.13 mm, the RL_{min} value of −54.11 dB is achieved at an incident frequency of 12.16 GHz. Compared with C_f@Fe_3O_4, the thinner matching thickness corresponds to the minimum reflection loss value. Meanwhile, an optimal EAB value of 6.24 GHz can be obtained at the matching thickness of 1.98 mm, in the frequency range of 11.76–18 GHz, covering the Ku band. Figure S9 in the ESM reveals the Cole–Cole curve of the C_f@FeS_2 nanocomposite, which shows more circles than the C_f@Fe_3O_4 nanocomposites, suggesting more Debye relaxation and more robust polarization loss capacity. Figure 6(c) exhibits the electromagnetic wave absorption performances of several Fe_3O_4- and FeS_2-based nanocomposites reported recently [25, 64–71]. As displayed, compared with other reported results, excellent RL_{min} and EAB values exist at a thinner matching thickness in the obtained C_f@FeS_2 nanocomposite, revealing its vast application potential serving as a high-efficiency and lightweight electromagnetic wave absorber.

For non-magnetic wave absorbing materials, the ability to attenuate incident electromagnetic waves mainly depends on the dielectric loss capacity. According to the Debye theory, ε'' can be classified into the conduction loss and polarization loss, which are usually obtained from Eq. (6) [72, 73]

$$\varepsilon'' = \varepsilon_p'' + \varepsilon_c'' = (\varepsilon_s - \varepsilon_\infty)\frac{2\pi f\tau}{1+(2\pi f)^2\tau^2} + \frac{\sigma}{2\pi f\varepsilon_0} \quad (6)$$

in which σ indicates the conductivity of the absorber, τ and ε_0 stand for the polarization relaxation time and vacuum dielectric constant, ε_c'' represents conduction loss, and ε_p'' refers to polarization loss, which can be regarded as an equivalent to a parallel circuit and a series circuit of resistance and capacitance and can be measured by fitting by nonlinear least squares [74, 75], respectively. Figure S10 in the ESM illustrates the electrical conductivity of the C_f, C_f@Fe_3O_4, and C_f@FeS_2 nanocomposites. The value of bare C_f was enhanced dramatically after decorating Fe_3O_4 nanoparticles and FeS_2 nanoparticles from 0.0113 to 0.0992 and 0.3294 S/m, respectively. Moreover, good electrical conductivity endows FeS_2 with outstanding conduction loss capacity, contributing to electromagnetic wave attenuation. For the purpose of elucidating the electromagnetic loss mechanism of C_f@FeS_2 nanocomposites, the conduction loss and polarization loss of C_f, C_f@Fe_3O_4-2#, and C_f@FeS_2 nanocomposites are shown in Figs. 6(d) and 6(e). As displayed in Fig. 6(d), the conduction loss value of each sample gradually decreases with increasing frequency, and the nanocomposites coated with iron-based compounds are noticeably better than pure carbon fibers. In the S and C bands, the conduction loss of C_f@FeS_2 nanocomposites is more than twice as high as that of C_f@Fe_3O_4-2# nanocomposites. In the X and Ku bands, the conduction loss values of C_f@Fe_3O_4-2# nanocomposites and C_f gradually decrease and are smaller than that of C_f@FeS_2 nanocomposites. It can be known from Fig. 6(e)

that the polarization loss of pure carbon fiber with a single component does not change dramatically with frequency, and that of C_f@Fe_3O_4-2# nanocomposites changes almost synchronously with that of C_f@FeS_2 nanocomposites in S and C bands, while the latter is significantly higher than the former in the X and Ku bands, which is consistent with the imaginary part curve of complex permittivity. Considering that, it is indicated that the C_f@FeS_2 nanocomposites obtain more robust conduction loss and polarization loss decaying ability in the Ku band. Figure 6(f) shows the attenuation constant of C_f@FeS_2 nanocomposite. The values are obviously larger than those of C_f@Fe_3O_4 nanocomposite, suggesting its stronger attenuation capacity for the incident electromagnetic wave under the action of outstanding conduction loss and polarization loss. Figure S11 in the ESM presents the $|Z_{in}/Z_0|$ value of C_f@FeS_2 nanocomposite, which is close to 1 at about 12.16 GHz, implying its proper impedance matching in medium-high frequency. Compared with C_f, C_f@Fe_3O_4 nanocomposites, in addition to retaining the dielectric loss and conduction loss properties of carbon fibers, possess additional eddy current loss and resonance loss effects from Fe_3O_4 magnetic nanoparticles, while the interfacial polarization caused by the heterogeneous interface between C_f and Fe_3O_4 also plays an important role in electromagnetic wave attenuation. According to above systematic characterization results, it can be inferred that the C_f@FeS_2 nanocomposite no longer possesses magnetic loss capability compared with C_f@Fe_3O_4 nanocomposites. However, its polarization loss and conduction loss are substantially enhanced. In other words, the enhanced effect of polarization loss has offset the reduced attenuation capability due to the sacrificial magnetic loss, as demonstrated in Fig. 6(g). Moreover, Fig. 6(h) displays several possible attenuation routes of the C_f@FeS_2 nanocomposite for the incident electromagnetic wave energy. Firstly, the overlapped and interlaced C_f constructs a network structure that not only provides some transmission paths for the incident electromagnetic wave, but also is conducive to multiple reflection/scattering and electronic migration on the surface of conductive fibers, which is crucial for improving the electromagnetic wave absorption performances [76, 77]. Secondly, the employment of FeS_2 nanoparticle brings enhanced conductivity and conductive loss than bare C_f and C_f@Fe_3O_4 nanocomposites. In the meanwhile, it also exerts strong effect on the enhancement of impedance matching and attenuation capacity of bare C_f [78]. In addition, there are a large number of interfaces between the C_f and FeS_2 nanoparticles, causing certain interface polarization and dipole polarization, and further effectively dissipating electromagnetic wave energy [79, 80].

4 Conclusions

In summary, the constructed network C_f@FeS_2 nanocomposite with excellent electromagnetic wave absorption performances was obtained by the electrospinning method based on the synthesis of C_f@Fe_3O_4 nanocomposites. Compared with the C_f@Fe_3O_4 intermediate, the magnetic loss of the C_f@FeS_2 nanocomposite is ineffective while the conduction loss and polarization loss have been ameliorated observably. Under the synergistic effect of the one-dimensional constructed network structure, carbon fiber defect-induced dipole polarization, interfacial polarization between C and FeS_2, as well as their excellent conductivity, the sample exhibits a strong absorption capability of −54.11 dB at 2.13 mm, while an optimal EAB value of 6.24 GHz, covering the entire Ku band, was also measured at a thickness of 1.98 mm. To conclude, they are superior to most reported nanofiber absorbers, indicating promising application prospect in the field of efficient electromagnetic wave absorption in the future.

Acknowledgements

The work reported here was supported by the National Natural Science Foundation of China (Nos. 52072196, 52002199, 52002200, and 52102106), the Major Basic Research Program of Natural Science Foundation of Shandong Province (No. ZR2020ZD09), the Natural Science Foundation of Shandong Province (Nos. ZR2019BEM042 and ZR2020QE063), the Innovation and Technology Program of Shandong Province (No. 2020KJA004), and the Taishan Scholars Program of Shandong Province (No. ts201511034). We express our grateful thanks to them for their financial support.

Electronic Supplementary Material: Supplementary material (further details of VSM, XPS, electromagnetic parameters, and so on) is available in the online version of this article at https://doi.org/10.1007/s12274-023-5776-x.

References

[1] Han, Y. X.; He, M. K.; Hu, J. W.; Liu, P. B.; Liu, Z. W.; Ma, Z. L.; Ju, W. B.; Gu, J. W. Hierarchical design of FeCo-based microchains for enhanced microwave absorption in C band. *Nano Res.* **2023**, *16*, 1773–1778.

[2] Li, N.; Huang, G. W.; Li, Y. Q.; Xiao, H. M.; Feng, Q. P.; Hu, N.; Fu, S. Y. Enhanced microwave absorption performance of coated carbon nanotubes by optimizing the Fe_3O_4 nanocoating structure. *ACS Appl. Mater. Interfaces* **2017**, *9*, 2973–2983.

[3] Chen, X. L.; Jia, Z. R.; Feng, A. L.; Wang, B. B.; Tong, X. H.; Zhang, C. H.; Wu, G. L. Hierarchical Fe_3O_4@carbon@MnO_2 hybrid for electromagnetic wave absorber. *J. Colloid Interfaces Sci.* **2019**, *553*, 465–474.

[4] Zhang, Y. L.; Kong, J.; Gu, J. W. New generation electromagnetic materials: Harvesting instead of dissipation solo. *Sci. Bull.* **2022**, *67*, 1413–1415.

[5] Wang, J.; Wu, X. Y.; Wang, Y. J.; Zhao, W. Y.; Zhao, Y.; Zhou, M.; Wu, Y.; Ji, G. B. Green, sustainable architectural bamboo with high light transmission and excellent electromagnetic shielding as a candidate for energy-saving buildings. *Nanomicro Lett.* **2022**, *15*, 11.

[6] Li, Z. J.; Wang, X. H.; Ling, H. L.; Lin, H.; Wang, T.; Zhang, M.; Meng, A. L.; Li, Q. D. Electromagnetic wave absorption properties of SiC@SiO_2 nanoparticles fabricated by a catalyst-free precursor pyrolysis method. *J. Alloys Compd.* **2020**, *830*, 154643.

[7] Zhang, Y. L.; Gu, J. W. A perspective for developing polymer-based electromagnetic interference shielding composites. *Nanomicro Lett.* **2022**, *14*, 89.

[8] Liu, Z. X.; Li, C. C.; Zhang, X. F.; Zhou, B. Z.; Wen, S. P.; Zhou, Y. F.; Chen, S. J.; Jiang, L.; Jerrams, S.; Zhou, F. L. Biodegradable polyurethane fiber-based strain sensor with a broad sensing range and high sensitivity for human motion monitoring. *ACS Sustainable Chem. Eng.* **2022**, *10*, 8788–8798.

[9] Gui, X. C.; Wang, K. L.; Wei, J. Q.; Lü, R. T.; Shu, Q. K.; Jia, Y.; Wang, C.; Zhu, H. W.; Wu, D. H. Microwave absorbing properties and magnetic properties of different carbon nanotubes. *Sci. China Ser. E Technol. Sci.* **2009**, *52*, 227–231.

[10] Zhang, M.; Ling, H. L.; Ding, S. Q.; Xie, Y. X.; Cheng, T. T.; Zhao, L. B.; Wang, T.; Bian, H. G.; Lin, H.; Li, Z. J. et al. Synthesis of CF@PANI hybrid nanocomposites decorated with Fe_3O_4 nanoparticles towards excellent lightweight microwave absorber. *Carbon* **2021**, *174*, 248–259.

[11] Meng, F. B.; Wang, H. G.; Huang, F.; Guo, Y. F.; Wang, Z. Y.; Hui, D.; Zhou, Z. W. Graphene-based microwave absorbing composites: A review and prospective. *Compos. B: Eng.* **2018**, *137*, 260–277.

[12] Cui, H. P.; Zhao, P. F.; Hu, B. X.; Long, A. C.; He, S. M.; Chen, G. J.; Liao, L. S.; Liao, J. H.; Zhao, Y. F. Sustainable microwave absorbing material based on macadamia nutshell derived porous carbon. *Nano* **2022**, *17*, 2250010.

[13] Li, Z. J.; Lin, H.; Xie, Y. X.; Zhao, L. B.; Guo, Y. Y.; Cheng, T. T.; Ling, H. L.; Meng, A. L.; Li, S. X.; Zhang, M. Monodispersed Co@C nanoparticles anchored on reclaimed carbon black toward high-performance electromagnetic wave absorption. *J. Mater. Sci. Technol.* **2022**, *124*, 182–192.

[14] Li, G.; Xie, T. S.; Yang, S. L.; Jin, J. H.; Jiang, J. M. Microwave absorption enhancement of porous carbon fibers compared with carbon nanofibers. *J. Phys. Chem. C* **2012**, *116*, 9196–9201.

[15] Huang, L. X.; Duan, Y. P.; Shi, Y. P.; Ma, X. R.; Pang, H. F.; Zeng, Q. W.; Che, R. C. Chiral asymmetric polarizations generated by bioinspired helical carbon fibers to induce broadband microwave absorption and multispectral photonic manipulation. *Adv. Opt. Mater.* **2022**, *10*, 2200249.

[16] Hu, Z.; Jin, S. L.; Lu, W. Z.; Tang, S.; Guo, C. T.; Lu, Y. G.; Zhang, R.; Liu, Y.; Jin, M. L. Effect of carbonization temperature on microwave absorbing properties of polyacrylonitrile-based carbon fibers. *Fuller. Nanotub. Carbon Nanostructures* **2017**, *25*, 637–641.

[17] Wang, W. W.; Yi, L. T.; Zheng, Y. Z.; Lu, J.; Jiang, A. S.; Wang, D. Photochromic and mechanochromic cotton fabric for flexible rewritable media based on acrylate latex with spiropyran cross-linker. *Comp. Commun.* **2023**, *37*, 101455.

[18] Xie, Y. X.; Guo. Y. Y.; Cheng, T. T.; Zhao, L. B.; Wang, T.; Meng, A. L.; Zhang, M.; Li, Z. J. Efficient electromagnetic wave absorption performances dominated by exchanged resonance of lightweight PC/Fe_3O_4@PDA hybrid nanocomposite. *Chem. Eng. J.* **2023**, *457*, 141205.

[19] Wang, L.; Ma, Z. L.; Qiu, H.; Zhang, Y. L.; Yu, Z.; Gu, J. W. Significantly enhanced electromagnetic interference shielding performances of epoxy nanocomposites with long-range aligned lamellar structures. *Nanomicro Lett.* **2022**, *14*, 224.

[20] Ning, M. Q.; Li, J. B.; Kuang, B. Y.; Wang, C. Z.; Su, D. Z.; Zhao, Y. J.; Jin, H. B.; Cao, M. S. One-step fabrication of N-doped CNTs encapsulating M nanoparticles (M = Fe, Co, Ni) for efficient microwave absorption. *Appl. Surf. Sci.* **2018**, *447*, 244–253.

[21] Han, B. H.; Chu, W. L.; Han, X. J.; Xu, P.; Liu, D. W.; Cui, L. R.; Wang, Y. H.; Zhao, H. H.; Du, Y. C. Dual functions of glucose induced composition-controllable Co/C microspheres as high-performance microwave absorbing materials. *Carbon* **2020**, *168*, 404–414.

[22] Zhou, X. F.; Jia, Z. R.; Zhang, X. X.; Wang, B. B.; Wu, W.; Liu, X. H.; Xu, B. H.; Wu, G. L. Controllable synthesis of Ni/NiO@porous carbon hybrid composites towards remarkable electromagnetic wave absorption and wide absorption bandwidth. *J. Mater. Sci. Technol.* **2021**, *87*, 120–132.

[23] Park, J. H.; Lee, S.; Ro, J. C.; Suh, S. J. Yolk–shell Fe-Fe_3O_4@C nanoparticles with excellent reflection loss and wide bandwidth as electromagnetic wave absorbers in the high-frequency band. *Appl. Surf. Sci.* **2022**, *573*, 151469.

[24] Ye, W.; Sun, Q. L.; Zhang, G. Y. Effect of heat treatment conditions on properties of carbon-fiber-based electromagnetic-wave-absorbing composites. *Ceram. Int.* **2019**, *45*, 5093–5099.

[25] Qiang, C. W.; Xu, J. C.; Zhang, Z. Q.; Tian, L. L.; Xiao, S. T.; Liu, Y.; Xu, P. Magnetic properties and microwave absorption properties of carbon fibers coated by Fe_3O_4 nanoparticles. *J. Alloys Compd.* **2010**, *506*, 93–97.

[26] Sun, Q. L.; Sun, L.; Cai, Y. Y.; Ji, T.; Zhang, G. Y. Activated carbon fiber/Fe_3O_4 composite with enhanced electromagnetic wave absorption properties. *RSC Adv.* **2018**, *8*, 35337–35342.

[27] Zhou, P. P.; Wang, X. K.; Wang, L. X.; Zhang, J.; Song, Z.; Qiu, X.; Yu, M. X.; Zhang, Q. T. Walnut shell-derived nanoporous carbon@Fe_3O_4 composites for outstanding microwave absorption performance. *J. Alloys Compd.* **2019**, *805*, 1071–1080.

[28] Zhao, J.; Wei, Y.; Zhang, Y.; Zhang, Q. G. 3D flower-like hollow CuS@PANI microspheres with superb X-band electromagnetic wave absorption. *J. Mater. Sci. Technol.* **2022**, *126*, 141–151.

[29] Zhang, Y. L.; Ma, Z. L.; Ruan, K. P.; Gu, J. W. Multifunctional $Ti_3C_2T_x$-(Fe_3O_4/polyimide) composite films with Janus structure for outstanding electromagnetic interference shielding and superior visual thermal management. *Nano Res.* **2022**, *15*, 5601–5609.

[30] Liu, X. X.; Liu, L. M.; Yan, W. W.; Wang, Y. F.; Huang, C. F.; Wang, Z. J. Hierarchical Fe_3O_4@FeS_2 nanocomposite as high-specific-capacitance electrode material for supercapacitors. *Energy Technol.* **2020**, *8*, 2000544.

[31] Xu, J.; Cui, Y. H.; Wang, J. Q.; Fan, Y. H.; Shah, T.; Ahmad, M.; Zhang, Q. Y.; Zhang, B. L. Fabrication of wrinkled carbon microspheres and the effect of surface roughness on the microwave absorbing properties. *Chem. Eng. J.* **2020**, *401*, 126027.

[32] Gou, G. J.; Meng, F. B.; Wang, H. G.; Jiang, M.; Wei, W.; Zhou, Z. W. Wheat straw-derived magnetic carbon foams: *In-situ* preparation and tunable high-performance microwave absorption. *Nano Res.* **2019**, *12*, 1423–1429.

[33] Zhou, X. F.; Zhang, C. H.; Zhang, M.; Feng, A. L.; Qu, S. L.; Zhang, Y.; Liu, X. H.; Jia, Z. R.; Wu, G. L. Synthesis of Fe_3O_4/carbon foams composites with broadened bandwidth and excellent electromagnetic wave absorption performance. *Compos. Part A Appl. Sci. Manuf.* **2019**, *127*, 105627.

[34] Li, Z. J.; Lin, H.; Ding, S. Q.; Ling, H. L.; Wang, T.; Miao, Z. Q.; Zhang, M.; Meng, A. L.; Li, Q. D. Synthesis and enhanced electromagnetic wave absorption performances of Fe_3O_4@C decorated walnut shell-derived porous carbon. *Carbon* **2020**, *167*, 148–159.

[35] Chen, G. Z.; Xu, D. W.; Chen, P.; Guo, X.; Yu, Q.; Qiu, H. F. Constructing and optimizing hollow bird-nest-patterned C@Fe_3O_4 composites as high-performance microwave absorbers. *J. Magn. Magn. Mater.* **2021**, *532*, 167990.

[36] Xu, J.; Liu, Z. H.; Li, Q.; Wang, Y. B.; Shah, T.; Ahmad, M.; Zhang, Q. Y.; Zhang, B. L. Wrinkled Fe_3O_4@C magnetic composite microspheres: Regulation of magnetic content and their microwave absorbing performance. *J. Colloid Interface Sci.* **2021**, *601*, 397–410.

[37] Jin, Y. H.; Luo, X.; Zhang, J. L.; Yu, Y. P.; An, J.; Zhang, J. F.; Zhao, D. L.; Gao, K. W. Electro-magnetic wave absorbing properties study of nano-composites based on Fe_3O_4. *Sci. Adv. Mater.* **2021**, *13*, 447–454.

[38] Ma, W. J.; He, P.; Wang, T. Y.; Xu, J.; Liu, X. Y.; Zhuang, Q. X.; Cui, Z. K.; Lin, S. L. Microwave absorption of carbonization temperature-dependent uniform yolk–shell H-Fe_3O_4@C microspheres. *Chem. Eng. J.* **2021**, *420*, 129875.

[39] Liang, C. B.; He, J.; Zhang, Y. L.; Zhang, W.; Liu, C. L.; Ma, X. T.; Liu, Y. Q.; Gu, J. W. MOF-derived CoNi@C-silver nanowires/cellulose nanofiber composite papers with excellent thermal management capability for outstanding electromagnetic interference shielding. *Compos. Sci. Technol.* **2022**, *224*, 109445.

[40] Yang, N.; Luo, Z. X.; Chen, S. C.; Wu, G.; Wang, Y. Z. Fe_3O_4 nanoparticle/N-doped carbon hierarchically hollow microspheres for broadband and high-performance microwave absorption at an ultralow filler loading. *ACS Appl. Mater. Interfaces* **2020**, *12*, 18952–18963.

[41] Zhan, Y. Q.; Long, Z. H.; Wan, X. Y.; Zhang, J. M.; He, S. J.; He, Y. 3D carbon fiber mats/nano-Fe_3O_4 hybrid material with high electromagnetic shielding performance. *Appl. Surf. Sci.* **2018**, *444*, 710–720.

[42] Zhang, K. C.; Zhang, Q.; Gao, X. B.; Chen, X. F.; Wang, Y.; Li, W. C.; Wu, J. Y. Effect of absorbers' composition on the microwave absorbing performance of hollow Fe_3O_4 nanoparticles decorated CNTs/graphene/C composites. *J. Alloys Compd.* **2018**, *748*, 706–716.

[43] Zhang, H. X.; Jia, Z. R.; Feng, A. L.; Zhou, Z. H.; Chen, L.; Zhang, C. H.; Liu, X. H.; Wu, G. L. *In-situ* deposition of pitaya-like Fe_3O_4@C magnetic microspheres on reduced graphene oxide nanosheets for electromagnetic wave absorber. *Compos. B: Eng.* **2020**, *199*, 108261.

[44] Zhang, S.; Jia, Z. R.; Zhang, Y.; Wu, G. L. Electrospun $Fe_{0.64}Ni_{0.36}$/MXene/CNFs nanofibrous membranes with multicomponent heterostructures as flexible electromagnetic wave absorbers. *Nano Res.* **2023**, *16*, 3395–3407.

[45] Zhang, Y. L.; Ruan, K. P.; Zhou, K.; Gu, J. W. Controlled distributed $Ti_3C_2T_x$ hollow microspheres on thermally conductive polyimide composite films for excellent electromagnetic interference shielding. *Adv. Mater.* **2023**, *35*, 2211642.

[46] Zhang, Z. Y.; Zhao, Y. H.; Li, Z.; Zhang, L. J.; Liu, Z. X.; Long, Z. K.; Li, Y. J.; Liu, Y.; Fan, R. H.; Sun, K. et al. Synthesis of carbon/SiO_2 core–sheath nanofibers with Co-Fe nanoparticles embedded in via electrospinning for high-performance microwave absorption. *Adv. Compos. Hybrid Mater.* **2022**, *5*, 513–524.

[47] Wang, Y. C.; Yao, L. H.; Zheng, Q.; Cao, M. S. Graphene-wrapped multiloculated nickel ferrite: A highly efficient electromagnetic attenuation material for microwave absorbing and green shielding. *Nano Res.* **2022**, *15*, 6751–6760.

[48] Wu, N. N.; Zhao, B. B.; Liu, J. Y.; Li, Y. L.; Chen, Y. B.; Chen, L.; Wang, M.; Guo, Z. H. MOF-derived porous hollow Ni/C composites with optimized impedance matching as lightweight microwave absorption materials. *Adv. Compos. Hybrid Mater.* **2021**, *4*, 707–715.

[49] Zhao, T. B.; Jia, Z. R.; Zhang, Y.; Wu, G. L. Multiphase molybdenum carbide doped carbon hollow sphere engineering: The superiority of unique double-shell structure in microwave absorption. *Small* **2023**, *19*, 2206323.

[50] Ye, Z. W.; Wang, K. J.; Li, X. Q.; Yang, J. J. Preparation and characterization of ferrite/carbon aerogel composites for electromagnetic wave absorbing materials. *J. Alloys Compd.* **2022**, *893*, 162396.

[51] Cheng, T. T.; Guo, Y. Y.; Xie, Y. X.; Zhao, L. B.; Wang, T.; Meng, A. L.; Li, Z. J.; Zhang, M. Customizing the structure and chemical composition of ultralight carbon foams for superior microwave absorption performance. *Carbon* **2023**, *206*, 181–191.

[52] Zhang, M.; Li, Z. J.; Wang, T.; Ding, S. Q.; Song, G. Y.; Zhao, J.; Meng, A. L.; Yu, H. Y.; Li, Q. D. Preparation and electromagnetic wave absorption performance of $Fe_3Si/SiC@SiO_2$ nanocomposites. *Chem. Eng. J.* **2019**, *362*, 619–627.

[53] Zhang, K. C.; Gai, X. Q.; Zhang, X. G.; Chen, X. F.; Li, H. X.; Zhao, X.; Chen, H.; Li, J. B. Preparation of nitrogen and sulfur co-doped graphene/Fe_3O_4/C nanocomposite and study on the absorbing properties. *J. Mater. Sci. Mater. Electron.* **2021**, *32*, 8807–8818.

[54] Fan, M. H.; Zhang, L. L.; Li, K. Q.; Liu, J. W.; Zheng, Y. N.; Zhang, L.; Song, S. Y.; Qiao, Z. A. FeS_2@C core–shell nanochains as efficient electrocatalysts for hydrogen evolution reaction. *ACS Appl. Nano Mater.* **2019**, *2*, 3889–3896.

[55] Pan, K. F.; Zhai, Y. Y.; Zhang, J. W.; Yu, K. FeS_2/C nanowires as an effective catalyst for oxygen evolution reaction by electrolytic water splitting. *Materials* **2019**, *12*, 3364.

[56] Lu, Z. X.; Wang, N. N.; Zhang, Y. H.; Xue, P.; Guo, M. Q.; Tang, B.; Xu, X.; Wang, W. X.; Bai, Z. C.; Dou, S. X. Metal–organic framework-derived sea-cucumber-like FeS_2@C nanorods with outstanding pseudocapacitive Na-ion storage properties. *ACS Appl. Energy Mater.* **2018**, *1*, 6234–6241.

[57] Man, Z. M.; Li, P.; Zhou, D.; Wang, Y. Z.; Liang, X. H.; Zang, R.; Li, P. X.; Zuo, Y. Q.; Lam, Y. M.; Wang, G. X. Two birds with one stone: FeS_2@C yolk–shell composite for high-performance sodium-ion energy storage and electromagnetic wave absorption. *Nano Lett.* **2020**, *20*, 3769–3777.

[58] Song, T. T.; Liu, Q.; Liu, J. Y.; Yang, W. L.; Chen, R. R.; Jing, X. Y.; Takahashi, K.; Wang, J. Fabrication of super slippery sheet-layered and porous anodic aluminium oxide surfaces and its anticorrosion property. *Appl. Surf. Sci.* **2015**, *355*, 495–501.

[59] Xu, Q. T.; Xue, H. G.; Guo, S. P. FeS_2 walnut-like microspheres wrapped with rGO as anode material for high-capacity and long-cycle lithium-ion batteries. *Electrochim. Acta* **2018**, *292*, 1–9.

[60] Liu, J. L.; Wang, M.; Zhang, L. M.; Zang, D. Y.; Liu, H.; Francesca Liotta, L.; Wu, H. J. Tunable sulfur vacancies and hetero-interfaces of FeS_2-based composites for high-efficiency electromagnetic wave absorption. *J. Colloid Interfaces Sci.* **2021**, *591*, 148–160.

[61] Van Nguyen, T.; Truong, N. T. N.; Ho, P.; Trinh, T. K.; Kim, J. H.; Park, C. Green and simple preparation of carbon-coated iron pyrite thin films for solar cells application. *J. Mater. Sci. Mater. Electron.* **2019**, *30*, 19752–19759.

[62] Zhu, Y. J.; Fan, X. L.; Suo, L. M.; Luo, C.; Gao, T.; Wang, C. S. Electrospun FeS_2@carbon fiber electrode as a high energy density cathode for rechargeable lithium batteries. *ACS Nano.* **2016**, *10*, 1529–1538.

[63] Wang, Q.; Liu, Z. Q.; Zhao, H. Y.; Huang, H.; Jiao, H.; Du, Y. P. MOF-derived porous Ni_2P nanosheets as novel bifunctional electrocatalysts for the hydrogen and oxygen evolution reactions. *J. Mater. Chem. A* **2018**, *6*, 18720–18727.

[64] Zhang, X.; Zhu, W. F.; Zhang, W. D.; Zheng, S. R.; Qi, S. H. Preparation of TiO_2/Fe_3O_4/CF composites for enhanced microwave absorbing performance. *J. Mater. Sci. Mater. Electron.* **2018**, *29*, 7194–7202.

[65] Liang, Y. Q.; Yin, X. Q.; Zhang, Y. Q.; Zheng, S. S.; Wu, Z. N.; Jia, H. Y.; Chen, Y. Electromagnetic response and microwave absorption properties of CF/Fe_3O_4 absorbing composites. *J. Mater. Sci. Mater. Electron.* **2022**, *33*, 2152–2165.

[66] Zhao, B.; Liang, L. Y.; Deng, J. S.; Bai, Z. Y.; Liu, J. W.; Guo, X. Q.; Gao, K.; Guo, W. H.; Zhang, R. 1D Cu@Ni nanorods anchored on 2D reduced graphene oxide with interfacial engineering to enhance microwave absorption properties. *CrystEngComm* **2017**, *19*, 6579–6587.

[67] Xing, L. S.; Li, X.; Wu, Z. C.; Yu, X. F.; Liu, J. W.; Wang, L.; Cai, C. Y.; You, W. B.; Chen, G. Y.; Ding, J. J. et al. 3D hierarchical local heterojunction of MoS_2/FeS_2 for enhanced microwave absorption. *Chem. Eng. J.* **2020**, *379*, 122241.

[68] Liao, Z. J.; Ma, M. L.; Tong, Z. Y.; Bi, Y. X.; Chung, K. L.; Qiao, M. T.; Ma, Y.; Ma, A. J.; Wu, G. L.; Li, Z. X. et al. Fabrication of one-dimensional $ZnFe_2O_4$@carbon@MoS_2/FeS_2 composites as electromagnetic wave absorber. *J. Colloid Interfaces Sci.* **2021**, *600*, 90–98.

[69] Wang, N.; Wang, Y.; Lu, Z.; Cheng, R. R.; Yang, L. Q.; Li, Y. F. Hierarchical core–shell FeS_2/Fe_7S_8@C microspheres embedded into interconnected graphene framework for high-efficiency microwave attenuation. *Carbon* **2023**, *202*, 254–264.

[70] Liu, C.; Wang, B. C.; Zhang, C.; Mu, C. P.; Wen, F. S.; Xiang, J. Y.; Nie, A. M.; Liu, Z. Y. Simple preparation and excellent microwave attenuation property of Fe_3O_4- and FeS_2- decorated graphene nanosheets by liquid-phase exfoliation. *J. Alloys Compd.* **2019**, *810*, 151881.

[71] Govindasamy, T.; Mathew, N. K.; Asapu, V. K.; Subramanian, V.; Subramanian, B. Investigation on evaluation of Fe_3S_4-carbon black nanohybrids for EMI shield in X-band region. *Diam. Relat. Mater.* **2023**, *131*, 109608.

[72] Li, Z. J.; Lin, H.; Wu, S. Y.; Su, X. Y.; Wang, T.; Zhao, W.; Jiang, Y. J.; Ling, H. L.; Meng, A. L.; Zhang, M. Rice husk derived porous carbon embedded with Co_3Fe_7 nanoparticles towards microwave absorption. *Compos. Sci. Technol.* **2022**, *229*, 109673.

[73] Wang, H. G.; Meng, F. B.; Huang, F.; Jing, C. F.; Li, Y.; Wei, W.; Zhou, Z. W. Interface modulating CNTs@PANi hybrids by controlled unzipping of the walls of CNTs to achieve tunable high-performance microwave absorption. *ACS Appl. Mater. Interfaces* **2019**, *11*, 12142–12153.

[74] Zhang, M.; Ling, H. L.; Wang, T.; Jiang, Y. J.; Song, G. Y.; Zhao, W.; Zhao, L. B.; Cheng, T. T.; Xie, Y. X.; Guo, Y. Y. et al. An equivalent substitute strategy for constructing 3D ordered porous carbon foams and their electromagnetic attenuation mechanism. *Nanomicro Lett.* **2022**, *14*, 157.

[75] Yang, H. J.; Cao, W. Q.; Zhang, D. Q.; Su, T. J.; Shi, H. L.; Wang, W. Z.; Yuan, J.; Cao, M. S. NiO hierarchical nanorings on SiC: Enhancing relaxation to tune microwave absorption at elevated temperature. *ACS Appl. Mater. Interfaces* **2015**, *7*, 7073–7077.

[76] Xu, H. L.; Yin, X. W.; Li, M. H.; Ye, F.; Han, M. K.; Hou, Z. X.; Li, X. L.; Zhang, L. T.; Cheng, L. F. Mesoporous carbon hollow microspheres with red blood cell like morphology for efficient microwave absorption at elevated temperature. *Carbon* **2018**, *132*, 343–351.

[77] Qiao, M. T.; Lei, X. F.; Ma, Y.; Tian, L. D.; He, X. W.; Su, K. H.; Zhang, Q. Y. Application of yolk–shell Fe_3O_4@N-doped carbon nanochains as highly effective microwave-absorption material. *Nano Res.* **2018**, *11*, 1500–1519.

[78] Cheng, J. Y.; Zhang, H. B.; Ning, M. Q.; Raza, H.; Zhang, D. Q.; Zheng, G. P.; Zheng, Q. B.; Che, R. C. Emerging materials and designs for low- and multi-band electromagnetic wave absorbers: The search for dielectric and magnetic synergy? *Adv. Funct. Mater.* **2022**, *32*, 2200123.

[79] Zhao, L. B.; Guo, Y. Y.; Xie, Y. X.; Cheng, T. T.; Meng, A. L.; Yuan, L. Y.; Zhao, W. X.; Sun, C. L.; Li, Z. J.; Zhang, M. Construction of SiC_{NWS}@$NiCo_2O_4$@PANI 1D hierarchical nanocomposites toward high-efficiency microwave absorption. *Appl. Surf. Sci.* **2022**, *592*, 153324.

[80] Jiang, Z. Y.; Si, H. X.; Li, Y.; Li, D.; Chen, H. H.; Gong, C. H.; Zhang, J. W. Reduced graphene oxide@carbon sphere based metacomposites for temperature-insensitive and efficient microwave absorption. *Nano Res.* **2022**, *15*, 8546–8554.